Piezoelectric Tweezer-type End-effector with Force- and Displacement-Sensing Capability

Yuichi Kurita, *Member, IEEE,* Fuyuki Sugihara,
Jun Ueda, *Member, IEEE,* and Tsukasa Ogasawara, *Member, IEEE*

***Abstract*—This paper presents the design and development of robotic tweezers with a force- and displacement-sensing capability driven by piezoelectric stack actuators. In order to satisfy sufficient stroke and tip-force for future medical operations, a rhombus strain amplification mechanism is adopted. One of the serially-connected piezoelectric stack actuators nested in the end-effector is used as a force sensor. The force-displacement characteristics at the outer-most layer with respect to the forces of the inner-most PZT actuators (i.e., forward model) is obtained from a lumped parameter model of the rhombus strain amplification mechanism and a Bernoulli-Euler beam model of the tweezer-style end-effector. The end-effector tip force and displacement is measured using an inverse model of the nested multi-layer structure relating these quantities to an induced voltage across the inner-most PZT actuator.**

The prototype end-effector has the size of 69 (length) $\times$ 14 (height) $\times$ 13 (width) [mm]. The performance test shows that the prototype has 1.0 [N] force and 8.8 [mm] displacement at the tip. The sensing accuracy was also evaluated through experiments. The experimental results show that the prototype has mean error of 0.086 [N] for force and 0.39 [mm] for displacement, which are equivalent to 11% of their maximum measurable values.

***Index Terms*—Robotic end-effector, Piezoelectric stack actuator, Sensing capability**

I. Introduction

The advantages of robot-assisted surgery are widely recognized [1]. Many robotic devices have been developed and tested for minimally invasive surgery and intervention. Providing force information to an operator, i.e., haptic feedback, is considered likely to improve the performance of tele-surgery; however, this has not been achieved yet in a fully practical fashion due to a lack of compact and high performance force sensors. Compact size is essential for minimally invasive surgery. Furthermore, ferromagnetic materials are impermissible for MRI use [2], [3], [4], [5], which greatly limits the choice of robot components.

Recent advances in both sensing and actuation technologies have produced exciting new ideas in the growing field of biomedical devices. Novel robotic and mechatronic devices used in biomedical systems require actuators that possess the following qualities: energy efficiency, compactness, low weight, high-speed, silent operations, and natural compliance. In recent years, great advances in actuation have been presented using, e.g., shape memory alloys [6], [7], pneumatic rubber actuators [8], [9], conductive polymers [10], and piezoelectric materials [11], [12]. These novel actuators are useful for multiple robotic applications, including human assistive technologies [13], [14] and other biomedical applications. Actuators using piezoelectric materials are also promising; they can be characterized by their high power density, high bandwidth, and high efficiency. The direct and converse piezoelectric effect make piezoelectric materials useful for both sensing and actuation [15], [16], [17], [18], [19]. A piezoelectric material generates electric charges on its surfaces when stress is applied. This effect, called "direct piezoelectric effect", enables one to use the material as a sensor that measures its strain, or displacement associated with the strain. The "converse piezoelectric effect," where the application of an electrical field creates mechanical deformation in the material, enables one to use the material as an actuator.

In this paper, a method to measure the tip-force of a tweezer-style piezoelectric end-effector without using additional sensors is presented. Piezoelectric stack actuators are serially connected and nested in a multi-layered strain amplification mechanism to create a large displacement at the tip of the end-effector. Conversely, the tip-force of the end-effector in contact with tissues/organs is estimated by measuring an induced voltage across one of the nested piezoelectric actuators. The idea is to use one of serially-connected piezoelectric stack actuators embedded in the end-effector as a force sensor. The force measurement capability is extremely important for medical applications because most tissues and organs are very soft and delicate [20], [21], [22], [23]. This sensor-equipped end-effector will provide not only haptic feedback functionality to the operator but also recording capability of surgical process. The "sensor-less" design would also contribute to simplification and miniaturization of the end-effector design.

The force-displacement characteristics at the outer-most layer with respect to the forces of the inner-most PZT actuators (i.e., forward model) can be obtained from a lumped parameter model of the rhombus strain amplification mechanism and a beam model of the tweezer-style end-effector. The key idea is to use an inverse model of the nested multi-layer structure to calculate the tip force and displacement from an induced voltage across the inner-most PZT actuator.

The remainder of this paper is organized as follows: in section II, a rhombus strain amplification mechanism and its lumped parameter model originally proposed by Ueda et al. [24] are briefly explained. The rhombus mechanism

Y. Kurita, F. Sugihara, and T. Ogasawara are with Graduate School of Information Science, Nara Institute of Science and Technology (NAIST), 8916-5, Takayama, Ikoma, Nara, 630-0192 Japan.

J. Ueda is with George W. Woodruff School of Mechanical Engineering, Georgia Institute of Technology, 801 Ferst Drive, Georgia Institute of Technology, Atlanta, GA 30332-0405, USA.

Manuscript received 2009.

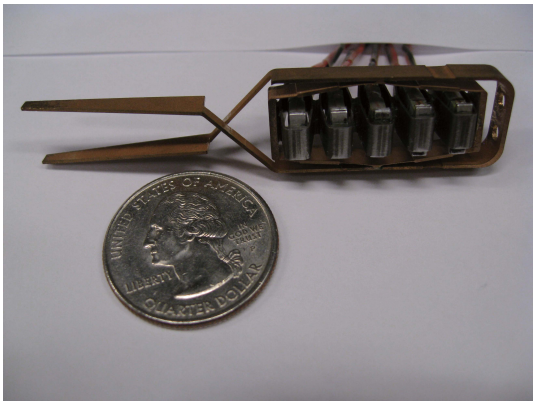

Fig. 1. Developed piezoelectric end-effector with force- and displacement-sensing capability

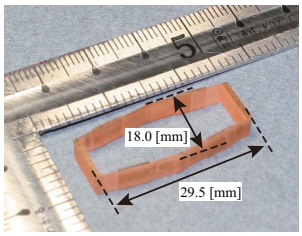

Fig. 2. Rhombus mechanism

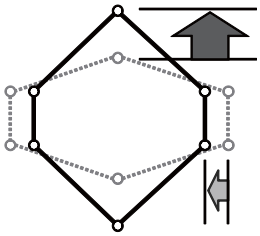

Fig. 3. Amplification principle

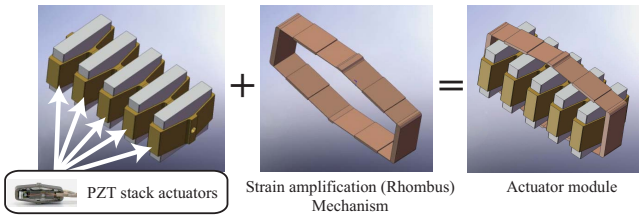

Fig. 4. Schematic assembly of nested rhombus multi-layer mechanism

is designed to satisfy desired performance. In section III, a tweezer-style end-effector is designed and fabricated (see Figure 1). In section IV, the inverse model of the nested structure is obtained. In section V, force and displacement sensing performance is evaluated.

II. Piezoelectric Actuators with Strain Amplification Mechanism

A. Overview of the Rhombus strain amplification mechanism

In this paper, the piezoelectric actuators are used to actuate an end-effector. Piezoelectric ceramics, such as lead zirconate titanate (PZT), have a high power density, high bandwidth, and high efficiency. The largest drawback of PZT is its extremely small strain, typically 0.1%. In order to generate a stroke large enough to drive the end-effector, a nested rhombus multi-layer mechanism [24] was adopted. Figure 2 shows an embodiment of the rhombus strain amplification mechanism. The mechanism is a rhombus-like hexagon that contracts in a longitudinal direction due to the contraction of the internal unit while it expands in the lateral direction (see Figure 3). A schematic assembly process is shown in Figure 4. Series of the PZT actuators were connected and nested in the rhombus amplification mechanism. This mechanism exhibits zero backlash and silent operation since no gears, bearings, or sliding mechanisms are used in the amplification structures. Figure 5 shows the assembled mechanism. Henceforth in this paper we shall call this assembled mechanism with PZT actuators and rhombus mechanism as "actuator module".

In the remainder of this section, the rhombus strain amplification mechanism and its lumped parameter model are briefly explained. For more detailed analysis and explanation, see [24].

B. Model of a Rhombus Mechanism [24]

Consider the mechanism shown in Figure 6 where a rhombus mechanism is connected to a spring load. k_{load} is the elastic modulus of the load, and k_{pzt} is the elastic modulus of the internal unit, such as a PZT stack actuator. Δx_{pzt} is the displacement of the internal unit, and f_{pzt} is the force applied to the amplification mechanism from the internal unit. f_1 is the force applied to the load by the actuator, and Δx_1 is the displacement of the load.

To illustrate the structural compliance, consider a lumped parameter model shown in Figure 7 with three spring elements, k_J , k_{BI}, k_{BO}, and one amplification leverage a. The three springs represent compliance of the mechanism: even if the displacement of the internal piezoelectric stack actuator is fixed, the end-point may move when an external force is applied to this point. This implies the existence of a spring element between the piezoelectric stack actuator and the end-point, which is represented by two serial springs k_{BO} and k_{BI}. In addition, if the piezoelectric stack actuator contracts, even when the external load is zero, the amplification mechanism creates a force opposed to this movement. This implies the existence of a spring element connected in parallel to the piezoelectric actuator, which is represented by k_J.

From Figure 7,

$$f_{pzt} + k_{BI}(\Delta x_c - \Delta x_{pzt}) - k_{pzt}\Delta x_{pzt} = 0 \quad (1)$$

$$ak_{BO}(a\Delta x_c - \Delta x_1) + k_J\Delta x_c + k_{BI}(\Delta x_c - \Delta x_{pzt}) = 0 \quad (2)$$

$$f_1 = k_{load}\Delta x_1 = k_{BO}(a\Delta x_c - \Delta x_1) \quad (3)$$

where Δx_c is the displacement at the connecting point between the leverage and the springs; however, this point is virtual and Δx_c does not correspond to a physical displacement.

From Equation (1) to (3), the relationship between f_{pzt} and Δx_1 is given by

$$\begin{aligned}(ak_{BI}k_{BO})f_{pzt} = \\ &[k_{load}\{a^2k_{BI}k_{IO} + k_{BI}k_J + k_{pzt}(a^2k_{BO} + k_J + k_{BI})\} \\ &+k_{BO}(k_{BI}k_J + k_{pzt}k_J + k_{BI}k_{pzt})] \cdot \Delta x_1. \end{aligned} \quad (4)$$

In this paper, multiple PZT actuators are used in the actuator module. Let N and n be the total number of the PZT actuators and the number of the energized actuators, respectively. Then we have

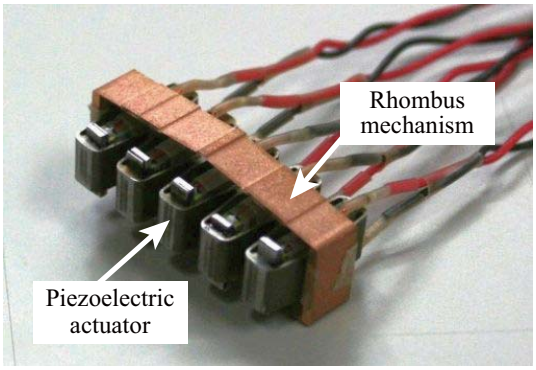

Fig. 5. Assembled actuator module. In this prototype, five PZT actuators are used.

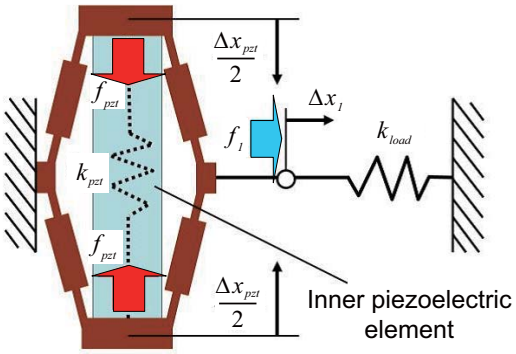

Fig. 6. Rhombus Mechanism with structural flexibilities [24]

$$\tilde{f}_1 = (k_{load} + \tilde{k_1}) \cdot \Delta x_1 \tag{5}$$

where

$$\tilde{k_1} = K_c \cdot \left(k_{BI}k_J + \frac{k_{pzt}}{N}(k_J + k_{BI}) \right) \tag{6}$$

$$\tilde{f}_1 = K_c \cdot ak_{BI} \cdot \frac{n}{N} f_{pzt} \tag{7}$$

where

$$K_c = k_{BO} \left(a^2 k_{BI}k_{BO} + k_{BI}k_J + \frac{k_{pzt}}{N}(a^2 k_{BO} + k_J + k_{BI}) \right)^{-1} \tag{8}$$

In the "blocked case" as shown in Figure 8 (a) where the output displacement is totally constrained, the force is largest. On the other hand, in the "free case" as shown in Figure 8 (b), the displacement is largest. From Equation (5) to (7), the largest force f_1^{max} and the largest displacement Δx_1^{max} can be given by

$$f_1^{max} = K_c \cdot ak_{BI} \cdot \frac{n}{N} f_{pzt}^{max} \tag{9}$$

$$\Delta x_1^{max} = \frac{ak_{BI}}{k_{BI}k_J + \frac{k_{pzt}}{N}(k_J + k_{BI})} \times \frac{n}{N} f_{pzt}^{max} \tag{10}$$

where f_{pzt}^{max} is the maximum force when all the PZT actuators are energized.

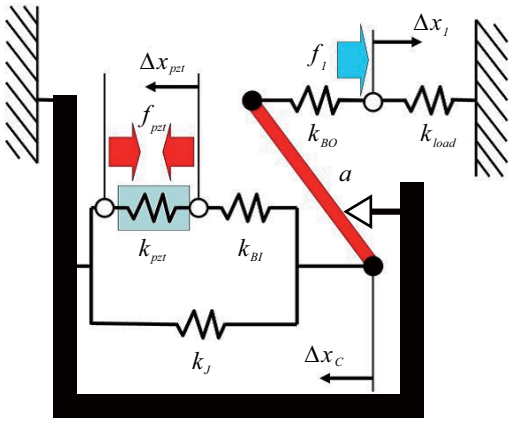

Fig. 7. Lumped parameter model of strain amplification mechanism [24]

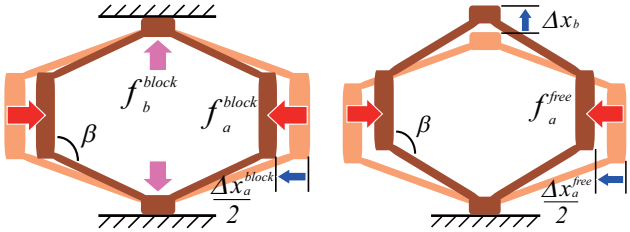

(a) blocked (b) free

Fig. 8. Deformation in blocked and free cases

C. Design of the Rhombus Mechanism

The four structural lumped parameters, i.e., a, k_{BI}, k_{BO}, and k_J, are calibrated by the displacements and forces from the blocked and free-load cases. Equation (1) to (3) give

$$k_{BI} = \frac{k_J \Delta x_b}{\Delta x_a^{free}} \cdot \left(a - \frac{\Delta x_b}{\Delta x_a^{free}} \right)^{-1} \tag{11}$$

$$k_{BO} = \frac{(k_{BI} + k_J) f_b^{block}}{\Delta x_a^{block}} \cdot \left(ak_{BI} - \frac{a^2 f_b^{block}}{\Delta x_a^{block}} \right)^{-1} \tag{12}$$

$$k_J = \frac{a f_a^{free}}{\Delta x_b}. \tag{13}$$

Leverage a is determined by using free-displacement characteristics and kinematic characteristics of the structure such as the angle of the oblique beam β, i.e., $\frac{\Delta x_b}{\Delta x_a^{free}} < a < \cot(\beta - \frac{\pi}{2})$. In this case, leverage a can be determined by

$$a = (1 - c)\cot\left(\beta - \frac{\pi}{2}\right) + c \cdot \frac{\Delta x_b}{\Delta x_a^{free}} \tag{14}$$

where $0 < c < 1$.

In this paper, the desired performance of the robotic end-effector is set to 1.0 [N] force and 10 [mm] displacement at the tip, which are determined to be comparable to the performance of one of Da Vinci's end-effectors and a surgical clip. Taking this into account, the dimensions of the rhombus mechanism are determined to satisfy $f_1 > 2.0$ [N] and $\Delta x_1 > 1.4$ [mm], using five PZT actuators ($N = 5$). Figure 9 shows the resulting rhombus mechanism. The maximum available force and displacement in this configuration are shown in the "Simulation" item of Table I.

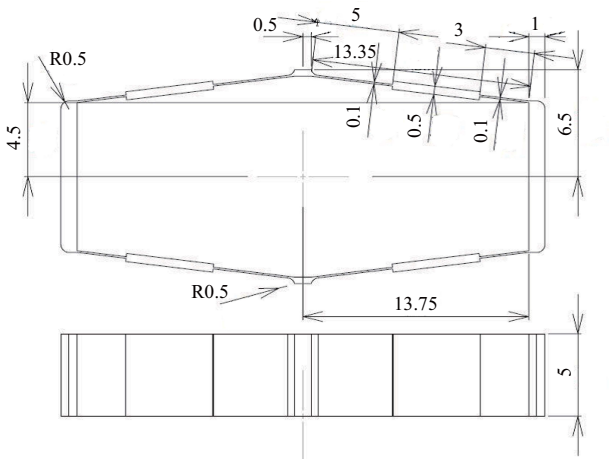

Fig. 9. Drawings of the strain amplification mechanism

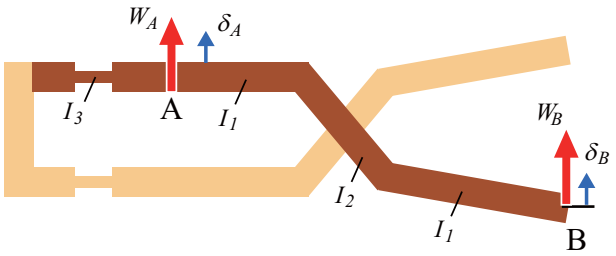

Fig. 10. Schematic model of the end-effector structure

D. Development and Experiment

The mechanism fabricated from phosphor bronze is shown in Figure 2. As is shown in Figure 4, five PZT actuators are connected in series and nested in the amplification mechanism. In this paper, PZT piezoelectric actuators with "moonie"-type [25], [26] amplification mechanism (APA35XS, CEDRAT, Inc.) were used. The specification of APA35XS is shown in Table II.

The performance of the actuator module developed here is evaluated by a force transducer and a laser displacement sensor. The results are shown in the "Experiment" item of Table I.

TABLE I
PERFORMANCE OF THE ACTUATOR MODULE

	Max. displacement [mm]	Max. force [N]
Simulation	1.48	2.58
Experiment	1.44	2.10

TABLE II
SPECIFICATION OF PZT STACK ACTUATOR (CEDRAT TECHNOLOGY INC.: APA35XS)

Height	Length	Width	Max. displacement	Max. force
5.5[mm]	13.25[mm]	5.0 [mm]	55 [μm]	27 [N]

III. TWEEZER-STYLE END-EFFECTOR WITH PZT ACTUATORS

A. Model of tweezer-style end-effector

The rhombus mechanism with a PZT actuators is nested into a tweezer-style end-effector with a reverse action mechanism. In this section, a Bernoulli-Euler beam model of the tweezer-style end-effector will be obtained.

The schematic model of the end-effector is shown in Figure 10. The displacement at the point A, i.e. δ_A, where the force from the actuator module is applied, and the displacement at the tip, i.e. δ_B, can be written as

$$\delta_A = \left(\frac{C_{A2}}{2EI_1} + \frac{C_{A4}}{2EI_3}\right) \cdot W_A + \left(\frac{C_{A1}}{2EI_1} + \frac{C_{A3}}{2EI_3}\right) \cdot W_B \quad (15)$$

$$\delta_B = \left(\frac{C_{B2}}{2EI_1} + \frac{C_{B5}}{2EI_3}\right) \cdot W_A + \left(\frac{C_{B1}}{2EI_1} + \frac{C_{B3}}{2EI_2} + \frac{C_{B4}}{2EI_3}\right) \cdot W_B \quad (16)$$

where W_A, W_B are the forces at the points A and B. E is Young's modulus of the phosphorus bronze, and I_1, I_2, I_3 are the second moment of area. $C_{A1} \sim C_{A4}$ and $C_{B1} \sim C_{B5}$ are coefficients obtained from Castigliano's theorem using a Bernoulli-Euler beam model of the tweezer-style end-effector (see appendix). Equation (15) and (16) will be used not only for determining the dimensions of the end-effector that achieves the desired performance but also for obtaining the inverse models that calculate the tip force and displacement from the force applied to the inner-most actuator unit.

B. Design and development

Let $\hat{W_A}$ be the force at the point A to achieve the desired tip displacement when the tip of the end-effector is free ($W_B = 0$). Then we have

$$\hat{W_A} = \left(\frac{C_{B2}}{2EI_1} + \frac{C_{B2}}{2EI_3}\right)^{-1} \cdot \hat{\delta_A}. \quad (17)$$

Here $\hat{\delta_A}$ is given from Equation (15).

The dimensions of the end-effector were designed by a simulation software so as to have the force and displacement as large as possible when taking the actuator module performance into account. Consequently, 1.1 [N] and 9.0 [mm] at the tip was obtained when the design shown in Figure 11. The stress analysis of the designed end-effector is shown in Figure 12. The maximum von Mises stress when the actuator module exerts the maximum force is 274 [MPa]. Since the yield stress of phosphor bronze is 528 [MPa], the end-effector designed has a sufficient strength.

The fabricated tweezer-style end-effector is shown in Figure 13. Figure 14 and Figure 15 shows the assembled end-effector nested actuator module described in section II. The dimensions are shown in Table III.

The performance test of the assembled end-effector was conducted using a force sensor and a laser displacement sensor. Figure 16 shows the force and displacement profiles when the input voltage alters from 0 to 150[V] and 150 to 0[V] in about 5 [sec] each. Table IV summarizes the results of the simulation and experiment. Finally, the prototype end-effector produces 1.0 [N] static pinching force and 8.8 [mm]

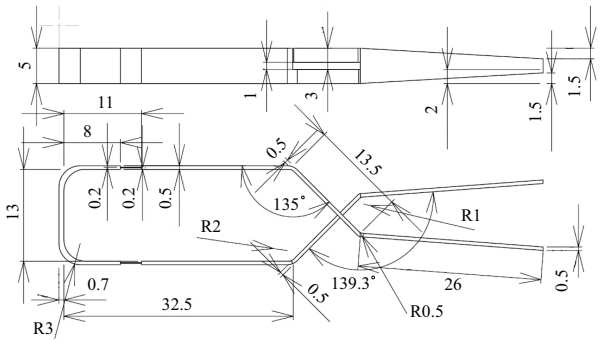

Fig. 11. Drawings of the tweezer-style end-effector

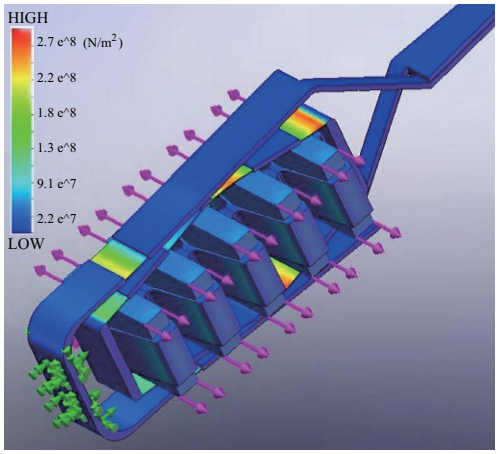

Fig. 12. Stress analysis of end-effector

displacement when providing 150[V] input voltage to the five PZT actuators. The natural frequency of the fabricated end-effector is 36[Hz]; uncompensated bandwidth of the actuation up to 35[Hz] was confirmed. This actuation bandwidth is greatly wider than existing robotic micro grippers driven by tendons or MRI-compatible manipulators driven by fluid actuators. The bandwidth could be further improved if a vibration compensation controller is implemented.

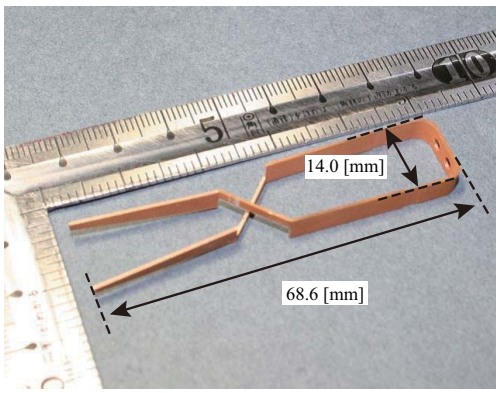

Fig. 13. Fabricated end-effector

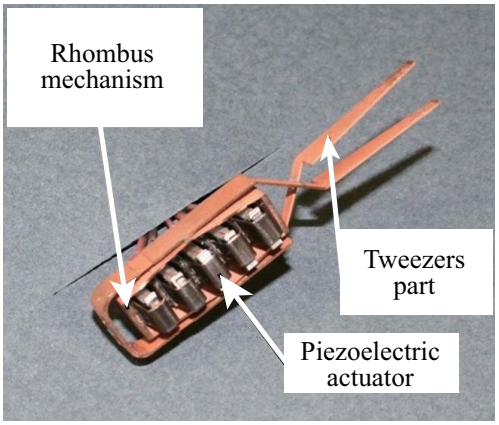

Fig. 14. Assembled end-effector nesting actuator module

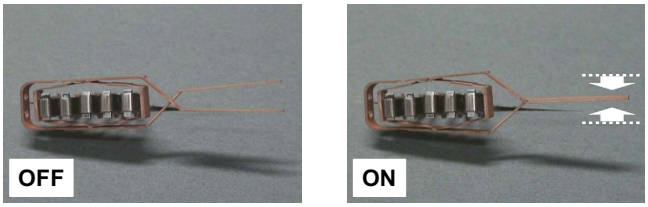

Fig. 15. Motion of the end-effector. The developed end-effector has a reverse action mechanism; the tips close when the actuators are energized.

IV. Sensing of Force and Displacement

A. Concept of force and displacement sensing

Force sensing capability without additional sensors can be realized by taking advantage of one of serially-connected PZT actuators as a force sensor. The lumped parameter models for the strain amplification mechanism and the Bernoulli-Euler beam model of the tweezer-style end-effector presented in section II-B and section III-A constitute the inverse models which can be used to determine the tip force and displacement from the voltage across a PZT stack.

B. Force-sensing circuit for a PZT actuator

The force sensing circuit was designed following traditional charge sensing circuits for the piezoelectric effect [27], [28], [29]. The circuit used in the experiment is shown in Figure 17. By measuring V_p and V_c, the applied force to a PZT actuator can be obtained:

TABLE III
Dimensions of the Assembled End-Effector

Length [mm]	68.6
Height [mm]	14.0
Width [mm]	13.25

TABLE IV
Performance of the Assembled End-Effector

	Displacement [mm]	Force [N]
Simulation	9.0	1.1
Experiment	8.8	1.0

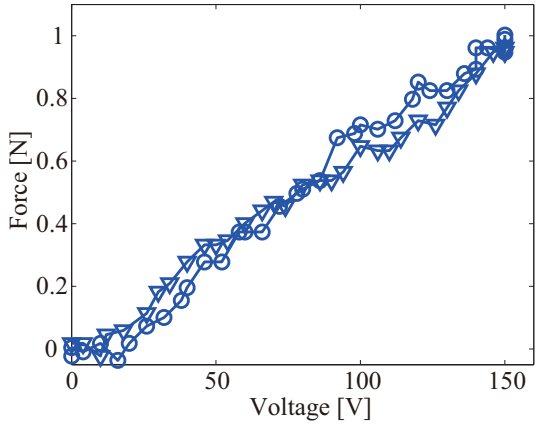

(a) Force profile

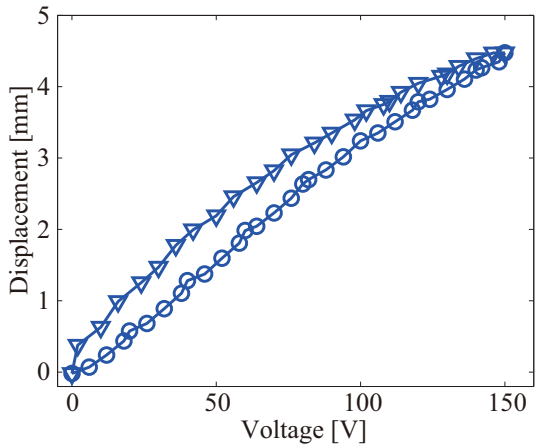

(b) Displacement profile (one side)

Fig. 16. Force and displacement performance. Circles are forward (from 0 to 150[V] in 5 [sec]) and inverse-triangles are backward (from 150 to 0[V] in 5 [sec]) directions.

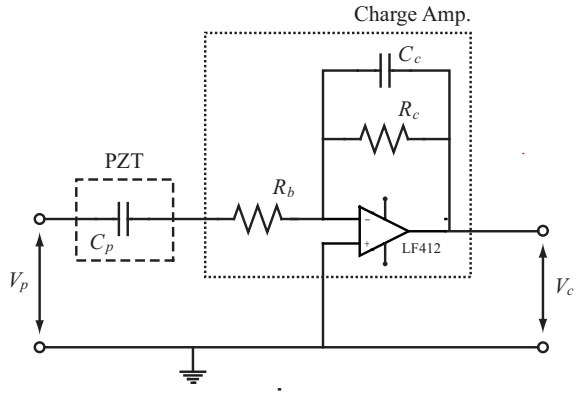

Fig. 17. Circuit chart for PZT charge sensing

$$f_s = K_s(C_p V_p + C_c V_c) \tag{18}$$

where K_s is the sensitivity of the piezoelectric effect. K_s can be obtained from Equation (18) by measuring the voltage V_p and V_c in the circuit when known forces are applied. In our configuration, $K_s = 4.3$ [N/μC] was obtained from the experiment.

The force sensing performance of a PZT actuator is shown in Figure 18. Table V shows the circuit parameters used in the experiment and Table VI summarizes the experimental results.

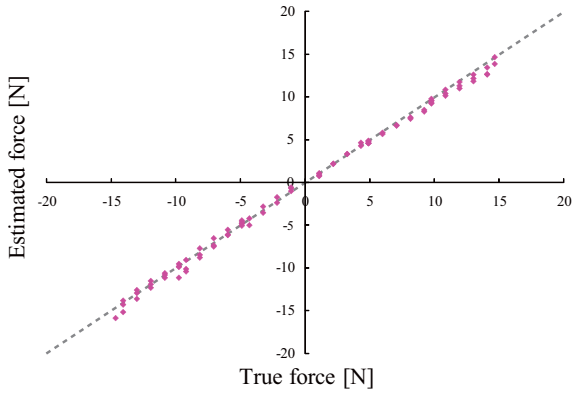

Fig. 18. Results of the force estimation by a PZT actuator and force sensing circuit

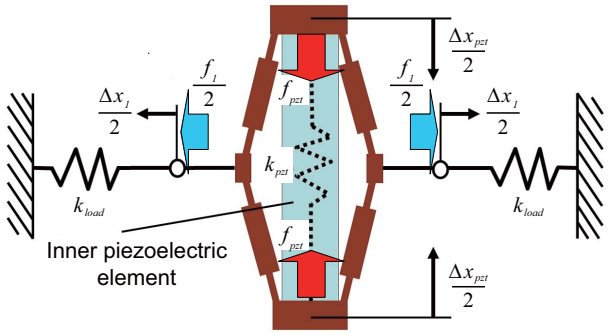

Fig. 19. Equivalent model of the end-effector

C. Inverse model for force sensing

The applied force to the PZT actuator used as a sensor can be written as

$$f_s = f_{pzt} - k_{pzt}\Delta x_{pzt}. \tag{19}$$

The rhombus mechanism can be described the lumped parameter model as shown in Figure 19. Since Figure 19 has a symmetric configuration, Equation (1) – (3) can be written as

TABLE V
CIRCUIT PARAMETERS

R_b [MΩ]	1.00
R_c [M Ω]	200
C_p [μ F]	0.41
C_c [μ F]	10.0

TABLE VI
RESULT OF THE FORCE SENSING EXPERIMENT

Maximum difference [N]	1.45
Minimum difference [N]	2.44×10^{-4}
RMSE [N]	0.54

$$f_{pzt} + k_{BI}(\Delta x_c - \Delta x_{pzt}) - k_{pzt}\Delta x_{pzt} = 0 \quad (20)$$

$$ak_{BO}\left(a\Delta x_c - \frac{\Delta x_1}{2}\right) + k_J\Delta x_c + k_{BI}(\Delta x_c - \Delta x_{pzt}) = 0 \quad (21)$$

$$\frac{f_1}{2} = k_{load}\frac{\Delta x_1}{2} = k_{BO}\left(a\Delta x_c - \frac{\Delta x_1}{2}\right) \quad (22)$$

where Δx_1 and f_1 are replaced by $\Delta x_1/2$ and $f_1/2$, respectively. From Equation (19) – (22),

$$f_s = \left(ak_{load} + \frac{k_J k_{load}}{ak_{BO}} + \frac{k_J}{a}\right)\cdot\frac{\Delta x_1}{2}. \quad (23)$$

Here we assume that f_{pzt} has a linear relationship with the input voltage V to the energized actuators:

$$f_{pzt} = \frac{f_{pzt}^{max}}{V_{max}}\cdot V. \quad (24)$$

From Equation (5), (20), (24), f_s can be given by

$$f_s = K_a \cdot V \quad (25)$$

$$K_a = \frac{n}{2N}\cdot\frac{ak_{BI}K_c}{k_{load}+k_1}\cdot\frac{f_{pzt}^{max}}{V_{max}}\left(ak_{load} + \frac{k_J k_{load}}{ak_{BO}} + \frac{k_J}{a}\right). \quad (26)$$

Here f_s can also be written as

$$f_s = f_s^{free} + f_s^{block} \quad (27)$$

where f_s^{free} and f_s^{block} are the forces applied to the PZT actuator for sensing when the tip of the end-effector is free and blocked, respectively. Let V_{free} denote the voltage when the tip is free. Then

$$f_s^{free} = K_a^{free}\cdot V_{free} \quad (28)$$

$$f_s^{block} = K_a^{block}\cdot(V - V_{free}) \quad (29)$$

where K_a^{free}, K_a^{block} are K_a when the tip is free and blocked, respectively.

Now Equation (30) follows from Equation (27)

$$V_{free} = \frac{K_a^{block}}{K_a^{block} - K_a^{free}}\cdot V - \frac{1}{K_a^{block} - K_a^{free}}\cdot f_a. \quad (30)$$

For force sensing, δ_B^{block}, which is the tip displacement when the tip is blocked, can be assumed to be zero. Then Equation (16) gives

$$W_B^{block} = \left(\frac{C_{B1}}{2EI_1} + \frac{C_{B3}}{2EI_2} + \frac{C_{B4}}{2EI_3}\right)^{-1} \times\left(\frac{C_{B2}}{2EI_1} + \frac{C_{B5}}{2EI_3}\right) W_A^{block} \quad (31)$$

where W_A^{block} and W_B^{block} are W_A and W_B when the tip is blocked. Here W_A^{block} satisfies

$$W_A^{block} = k_{load}^{block}\cdot\delta_A^{block}. \quad (32)$$

In Figure 19, Δx_1 equals to $2\delta_A$. Therefore, Equation (23) and (29) give

$$\delta_A^{block} = K_a^{block}\left(ak_{load}^{block} + \frac{k_J k_{load}^{block}}{ak_{BO}} + \frac{k_J}{a}\right)^{-1}(V - V_{free}). \quad (33)$$

Thus, the inverse model for the force sensing can be obtained from Equation (31) – (33) as

$$\begin{aligned} W_B &= K_a^{block}\, k_{load}^{block}\left(\frac{C_{B2}}{2EI_1} + \frac{C_{B5}}{2EI_3}\right) \\ &\times\left(\frac{C_{B1}}{2EI_1} + \frac{C_{B3}}{2EI_2} + \frac{C_{B4}}{2EI_3}\right)^{-1} \\ &\times\left(ak_{load}^{block} + \frac{k_J k_{load}^{block}}{ak_{BO}} + \frac{k_J}{a}\right)^{-1} \\ &\times\left(-\frac{K_a^{free}}{K_a^{block} - K_a^{free}}V + \frac{1}{K_a^{block} - K_a^{free}}\cdot f_s\right) \end{aligned} \quad (34)$$

D. Inverse model for displacement sensing

For displacement sensing, $W_B^{free} = 0$ can be assumed because the tip is free. Then Equation (16) gives

$$\delta_B^{free} = \left(\frac{C_{A2}}{2EI_1} + \frac{C_{A4}}{2EI_3}\right)\cdot W_A^{free}. \quad (35)$$

W_A^{free}, which is W_A when the tip is free, satisfies

$$W_A^{free} = k_{load}^{free}\cdot\delta_A^{free}. \quad (36)$$

Equation (23) and (28) give

$$\delta_A^{free} = K_a^{free}\left(ak_{load}^{free} + \frac{k_J k_{load}^{free}}{ak_{BO}} + \frac{k_J}{a}\right)^{-1} V_{free}. \quad (37)$$

(38)

Thus, the inverse model for the displacement sensing can be obtained from Equation (35) – (37) as

$$\begin{aligned} \delta_B &= K_a^{free}\, k_{load}^{free}\left(\frac{C_{A2}}{2EI_1} + \frac{C_{A4}}{2EI_3}\right) \\ &\times\left(ak_{load}^{free} + \frac{k_J k_{load}^{free}}{ak_{BO}} + \frac{k_J}{a}\right)^{-1} \\ &\times\left(\frac{K_a^{block}}{K_a^{block} - K_a^{free}}V - \frac{1}{K_a^{block} - K_a^{free}}\cdot f_s\right). \end{aligned} \quad (39)$$

V. Experiment and discussion

The overview of the force estimation experiment is shown in Figure 20. Figure 21 shows the experimental results of the force and displacement estimations when the input voltage cycles from 0 to 150 [V] (forward) and 150 to 0 [V] (backward). In this experiment, the force was measured under the blocked condition where the tip of the end-effector is in contact with a force transducer. On the other hand, the displacement was measured under the free condition using a non-contact laser position sensor. The estimation errors are summarized in Table VII. The accuracy is 12% (forward) and 9.8% (backward) for

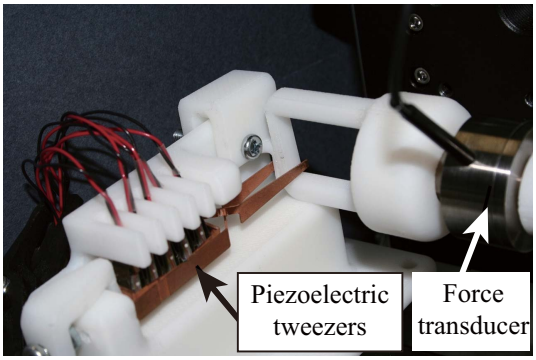

Fig. 20. Overview of the force estimation experiment

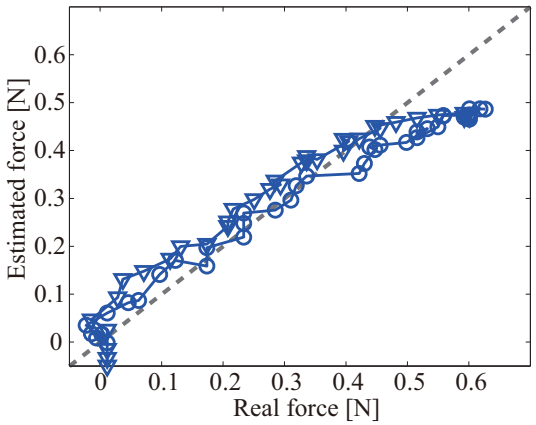

(a) Force estimation

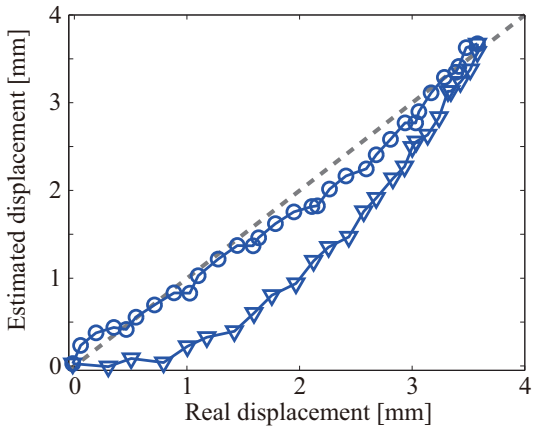

(b) Displacement estimation

Fig. 21. Result of displacement and force estimation. Circles are forward (from 0 to 150[V]) and inverse-triangles are backward (from 150 to 0[V]) directions.

the force sensing, and 4% (forward) and 18% (backward) for the displacement sensing.

The total accuracy is 11% of the maximum measurable values for both displacement and force sensing.

One possible reason for the hysteresis is the characteristics of the PZT actuator. In general, PZT actuators have hysteresis between the input voltage and their deformation. In this paper, the relationship between the input voltage and the force generated by the PZT actuator was modeled by a linear function. This could be responsible for the estimation error.

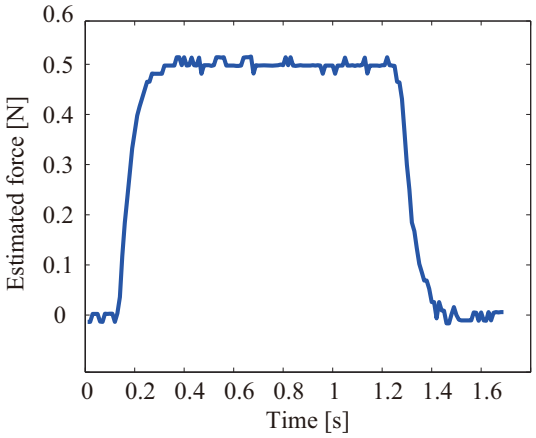

Fig. 22. Force measurement under 0.5 [N] force is applied

Figure 22 shows the force profile estimated when 0.5 [N] is statically applied for about 1 [sec]. This figure shows the estimated force is stable and successfully goes back to zero when unloaded. This indicates there is not significant charge loss and bias. However, charge loss and bias issues might occur when the device is used for a very long time. In such cases, periodic charge resets would be necessary to maintain the sensing accuracy.

The sensing accuracy could be improved by using traditional methods to improve hysteresis characteristics of PZT actuators, e.g., using model functions obtained by experiments [30]; applying an electric charge [31]; observing an induced charge [32]. Applying a very low increasing- and decreasing-rate input-voltage to the PZT actuators also would improve the hysteresis.

VI. Conclusion

This paper presented a tweezer-type end-effector with displacement- and force-sensing capability. The end-effector is actuated by PZT piezoelectric stack actuators with a rhombus strain amplification mechanism. The inverse models of the nested multi-layer structure that calculate the tip force and displacement were obtained from a lumped parameter model of the rhombus strain amplification mechanism and a beam model of the tweezer-style end-effector.

The dimensions of the end-effector were determined by taking the elastic properties of both the actuators and end-effector mechanism into account. The prototype has a size of 69

TABLE VII
Mean Error of Estimation

Mean Error	Forward	Backward	Total
Force [N]	0.094 12[%]	0.078 9.8[%]	0.086 11[%]
Displacement [mm]	0.14 4.0[%]	0.63 18[%]	0.39 11[%]
Std. Dev.	Forward	Backward	Total
Force [N]	0.066	0.051	0.061
Displacement [mm]	0.10	0.32	0.33

(length) × 14 (height) × 13 (width) [mm]. The performance of the prototype was tested by simulation and experiments. We confirmed that the prototype has 1.0 [N] blocked force and 8.8 [mm] free displacement at the tip. We also evaluated the accuracy of the force and displacement measurement. The mean errors were 0.086 [N] for force and 0.39 [mm] for displacement sensing, which are equivalent to 11% of their maximum measurable values. Sophistication and improvement of the end-effector model, the force-sensing circuit, and the hysteresis characteristics of the PZT actuators will enhance the sensing accuracy.

The force/displacement requirements in actual surgical applications depend on tasks and situations. For example, endoscopic hemostatic clipping devices have 9-12 [mm] for their jaw opening width [33]. Also endoscopic surgery generally requires over 1 [N] for hemostatic clips, 1-5 [N] for suture tying, 2-5 [N] for tool grasping and tissue cutting, and 10 [N] for securely holding [34], [35]. Additionally, an easily washable structure is required when the proposed end-effector is to be used as a surgical tool. Careful shields of electric leads and actuators are necessary to obtain the MRI compatibility that allows the MRI-guided surgery. The dimensions of the end-effector should also be miniaturized to minimize the aperture radius when considering applications in laparoscopic and endoscopic surgeries. These issues would be taken into account in our next version.

REFERENCES

[1] R. H. Taylor and D. Stoianovici. Medical robotics in computer-integrated surgery. *IEEE transactions on robotics and automation*, 19(5):765–781, 2003.

[2] J. F. Schenck. The role of magnetic susceptibility in magnetic resonance imaging: Mri magnetic compatibility of the first and second kinds. *Medical Physics*, 23(6):815–850, 1996.

[3] K. Chinzei and K. Miller. Mri guided surgical robot. In *Proc. of Australian Conference on Robotics and Automation*, pages 50–55, 2001.

[4] R. Gassert, D. Chapuis, H. Bleuler, and E. Burdet. Sensors for applications in magnetic resonance environments. *IEEE/ASME Transactions on Mechatronics*, 13(3):335–344, 2008.

[5] S. M. Mirsattari, C. Davies-Schinkel, G. B. Young, M. D. Sharpe, J. R. Ives, and D. H. Lee. Usefulness of a 1.5 t mri-compatible eeg electrode system for routine use in the intensive care unit of a tertiary care hospital. *Epilepsy Research*, 84(1):28–32, 2009.

[6] A. Srinivasan, D. McFarland, H. Canistraro, and E. Begg. Multiplexing embedded niti-nol actuators to obtain increased bandwidth in structural control. *Journal of intelligent material systems and structures*, 8(3):202–214, 1997.

[7] Y. Fu, H. Du, W. Huang, S. Zhang, and M. Hu. Tini-based thin films in mems applications: a review. *Sensors and actuators A, Physical*, 112(2–3):395–408, 2004.

[8] A. Sanchez, V. Mahout, and B. Tondu. Nonlinear parametric identification of a mckibben artificial pneumatic muscle using flatness property of the system. In *Proc. of the 1998 IEEE International Conference on Control Applications*, 1998.

[9] D. Caldwell. Biomimetic actuators in prosthetic and rehabilitation applications. *Technology and Health Care*, 10(2):107–120, 2002.

[10] S. Hara, T. Zama, W. Takashima, and K. Kaneto. Artificial muscles based on polypyrrole actuators with large strain and stress induced electrically. *Polymer journal*, 36(3):151–161, 2004.

[11] K. Uchino. *Piezoelectric Actuators and Ultrasonic Motors*. Kluwer Academic Publishers, 1997.

[12] Y. Mamiya. Applications of piezoelectric actuator. *NEC Technical Journal*, 1(5):82–86, 2006.

[13] J. Ueda, M. Matsugashita, R. Oya, and T. Ogasawara. Control of muscle force during exercise using a musculoskeletal-exoskeletal integrated human model. *Experimental Robotics*, pages 143–152, 2008.

[14] J. Ueda, D. Ming, V. Krishnamoorthy, M. Shinohara, and T. Ogasawara. Individual muscle control using an exoskeleton robot for muscle function testing. *IEEE Transactions on Neural Systems and Rehabilitation Engineering*, 18(4):339–350, 2010.

[15] J. Tansocka and C.C. Williamsa. Force measurement with a piezoelectric cantilever in a scanning force microscope. *Ultramicroscopy*, 42–44(2):1464–1469, 1992.

[16] C. Niezrecki, D. Brei, S. Balakrishnan, and A. Moskalik. Piezoelectric actuation: State of the art. *The Shock and Vibration Digest*, 33(4), 2001.

[17] T. Shimizu, M. Shikida, K. Sato, K. Itoigawa, and Y. Hasegawa. Micromachined active tactile sensor for detecting contact force and hardness of an object. In *Proc. of International Symposium on Micromechatronics and Human Science*, pages 67–71, 2002.

[18] P. Ronkanen, P. Kallio, and H. N. Koivo. Simultaneous actuation and force estimation using piezoelectric actuators. In *Proc. of International Conference on Mechatronics and Automation*, pages 3261–3265, 2007.

[19] S. Nurung, K. C. Magsino, and I. Nilkhamhang. Force estimation using piezoelectric actuator with adaptive control. In *Proc. of International Conference on Electrical Engineering/Electronics, Computer, Telecommunications and Information Technology*, pages 350–353, 2009.

[20] T. Kawahara, S. Tanaka, and M. Kaneko. Non-contact stiffness imager. *The International Journal of Robotics Research*, 25(5-6):537–549, 2006.

[21] S. Shostek, C. Ho, D. Kalanovic, and M. O. Schurr. Artificial tactile sensing in minimally invasive surgery: a new technical approach. *Minimally Invasive Therapies Allied Technologies*, 15(5):296–304, 2006.

[22] M.S. Ju, H. M. Vong, C.C. K. Lin, and S.F. Ling. Development of soft tissue stiffness measuring device for minimally invasive surgery by using sensing cum actuating method. In *Proc. of 13th International Conference on Biomedical Engineering*, volume 23, pages 291–295, 2009.

[23] T. Takaki, Y. Omasa, I. Ishii, T. Kawahara, , and M. Okajima. Force visualization mechanism using a moir ´ e fringe applied to endoscopic surgical instruments. In *Proc. of the IEEE International Confence on Robotics and Automation*, pages 3648–3653, 2010.

[24] J. Ueda, T. W. Secord, and H. H. Asada. Large effective-strain piezoelectric actuators using nested cellular architecture with exponential strain amplification mechanisms. *IEEE/ASME Transactions on Mechatronics*, 15(5):770–782, 2010.

[25] R. Newnham, A. Dogan, Q. Xu, K. Onitsuka, J. Tressler, and S. Yoshikawa. Flextensional moonie actuators. In *Proc. of IEEE Ultrasonics Symposium*, pages 509–513, 1993.

[26] R. Leletty and F. R. Claeyssen. New amplified piezoelectric actuator for precision positioning and active damping. In *Proc. Smart Structures and Materials SPIE*, volume 3041, pages 496–504, 1997.

[27] M. Fukunaga and Y. Uesu. Compact and simple apparatus for measuring direct piezoelectricity. *Japanese Journal of Applied Physics*, 42(9B):6115–6117, 2003.

[28] K. Imoto, M. Nishiura, K. Yamamoto, M. Date, E. Fukuda, and Y. Tajitsu. Elasticity control of piezoelectric lead zirconate titanate (pzt) materials using negative-capacitance circuits. *Japanese Journal of Applied Physics*, 44(9B):7019–7023, 2005.

[29] J. Kim and C. Yim. An impact force compensation algorithm based on a piezo force sensor for wire bonding processes. *Control Engineering Practice*, 16:685–696, 2008.

[30] C. V. Newcomb and I. Flinn. Improving the linearlity of piezoelectric ceramic actuators. *Electronics Letters*, 18:442–444, 1982.

[31] Ge P and M. Jouaneh. Modeling hysteresis in piezoceramic actuators. *Precision Engineering*, 17(3):211–221, 1995.

[32] K. Furutani and N. Ohta. Displacement monitoring of stacked piezoelectric actuator by observing induced charge. *International Journal of Automation Technology*, 2(1):12–17, 2008.

[33] Technology status evaluation report: Endoscopic hemostatic devices. *Gastrointestinal Endoscopy*, 69(6):987–996, 2009.

[34] S-K. Kim, W-H Shin, S-Y. Ko, J. Kim, and D-S Kwon. Design of a compact 5-dof surgical robot of a spherical mechanism: Cures. In *Proc. of the IEEE/ASME International Conference on Advanced Intelligent Mechatronics*, pages 990–995, 2008.

[35] L. van den Bedem, R. Hendrix, N. Rosielle, M. Steinbuch, and H. Nijmeijer. Design of a minimally invasive surgical teleoperated master-slave system with haptic feedback. In *Proc. of the International Conference on Mechatronics and Automation*, pages 60–65, 2009.

APPENDIX

Figure 23 shows a schematic diagram of the end-effector. Here we assume the end-effector is fixed at point C and the force generated from the actuator module is applied at the

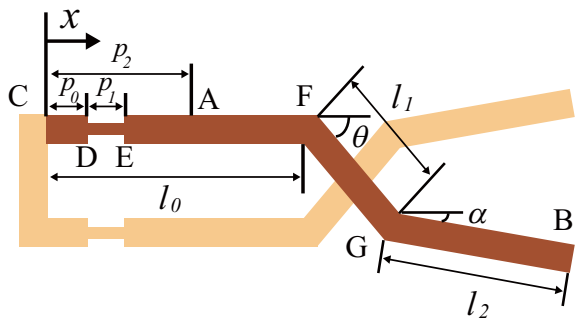

Fig. 23. Schematic of the end-effector

point A. From Castigliano's theorem using a Bernoulli-Euler beam model, $C_{A1} \sim C_{A4}$ and $C_{B1} \sim C_{B5}$ in Equation (15) and Equation (16) can be written as follows:

$$\begin{aligned}
C_{A1} = & -\tfrac{2}{3}\left\{p_0^3 + (p_2 - p_0 - p_1)^3\right\} \\
& + (l_0 + l_1\cos\theta + l_2\cos\alpha)p_0(p_0 - 2p_2) + p_2p_0^2 \\
& - (l_0 + l_1\cos\theta + l_2\cos\alpha - p_0 - p_1)(p_2 - p_0 - p_1)^2 \\
& + (p_2 - p_0 - p_1)^3 \qquad (40) \\
C_{A2} = & \tfrac{2}{3}\left\{p_0^3 + (p_2 - p_0 - p_1)^3\right\} \\
& + 2p_2p_0(p_2 - p_0) \qquad (41) \\
C_{A3} = & -\tfrac{2}{3}p_1^3 + (p_2 - p_0)p_1^2 \\
& + (l_0 + l_1\cos\theta + l_2\cos\alpha - p_0)p_1(p_1 - 2p_2 + 2p_0) \qquad (42) \\
C_{A4} = & \tfrac{2}{3}p_1^3 + 2(p_2 - p_0)p_1(a - p_0 - p_1) \qquad (43) \\
C_{B1} = & \tfrac{2}{3}\left\{p_0^3 + (p_2 - p_0 - p_1)^3\right\} \\
& + \tfrac{2}{3}(l_0 - p_2)^3 + \tfrac{2}{3}l_2^3\cos^3\alpha \\
& + 2p_0(l_0 + l_1\cos\theta + l_2\cos\alpha) \\
& \times (l_0 + l_1\cos\theta + l_2\cos\alpha - p_0) \\
& + 2(l_0 + l_1\cos\theta + l_2\cos\alpha - p_0 - p_1)(p_2 - p_0 - p_1) \\
& \times (l_0 + l_1\cos\theta + l_2\cos\alpha - p_2) \\
& + 2(l_0 - p_2)(l_0 + l_1\cos\theta + l_2\cos\alpha - p_2) \\
& \times (l_1\cos\theta + l_2\cos\alpha) \qquad (44) \\
C_{B2} = & -\tfrac{2}{3}\left\{p_0^3 + (p_2 - p_0 - p_1)^3\right\} \qquad (45) \\
& + p_2p_0^2 + (p_2 - p_0 - p_1)^3 \\
& + p_0(l_0 + l_1\cos\theta + l_2\cos\alpha)(p_0 - 2p_2) \\
& - (l_0 + l_1\cos\theta + l_2\cos\alpha - p_0 - p_1) \\
& \times (p_2 - p_0 - p_1)^2 \qquad (46) \\
C_{B3} = & \tfrac{2}{3}l_1^3\cos^3\theta \\
& + 2l_1\cos\theta l_2\cos\alpha(l_1\cos\theta + l_2\cos\alpha) \qquad (47) \\
C_{B4} = & \tfrac{2}{3}p_1^3 + 2p_1(l_0 + l_1\cos\theta + l_2\cos\alpha - p_0) \\
& \times (l_0 + l_1\cos\theta + l_2\cos\alpha - p_0 - p_1) \qquad (48) \\
C_{B5} = & -\tfrac{2}{3}p_1^3 + (p_2 - p_0)p_1^2 \\
& + p_1(l_0 + l_1\cos\theta + l_2\cos\alpha - p_0)(p_1 - 2p_2 + 2p_0) \qquad (49)
\end{aligned}$$

where p_0, p_1, p_2 are the lengths between C and D, D and E, C and A respectively, l_0, l_1, l_2 are the lengths between C and F, F and G, G and B respectively, and θ, α are the angles shown in Figure 23.

PLACE PHOTO HERE

Yuichi Kurita received the B.E. degree from Osaka University, Osaka, Japan in 2000, and the M.E. and Ph.D degrees from Nara Institute of Science and Technology (NAIST), Nara, Japan, in 2002 and 2004, respectively, all in information science. From 2005 to 2007, he was with Graduate School of Engineering, Hiroshima University, Hiroshima, Japan. In 2007, he joined NAIST, and is currently an assistant professor of Robotics Laboratory in Graduate School of Information Science. From 2010, he is a visiting scholar in George W. Woodruff School of Mechanical Engineering, Georgia Institute of Technology, USA. His research interests include human analysis/modeling, bio-robotics, and medical engineering.

PLACE PHOTO HERE

Fuyuki Sugihara received the B.E degree from Kyoto Institute of Technology, Kyoto, Japan in 2006, and M.E. degree from Nara Institute of Science and Technology (NAIST), Nara, Japan in 2008. His research interests include robotics and mechatronics.

PLACE PHOTO HERE

Jun Ueda Biography text here.

PLACE PHOTO HERE

Tsukasa Ogasawara received the B.E., M.E., and Ph.D. degrees from The University of Tokyo, Tokyo, Japan, in 1978, 1980, and 1983, respectively. From 1983 to 1998, he was with the Electorotechnical Laboratory, Ministry of International Trade and Industry, Japan. From 1993 to 1994, he was with the Institute for Real-Time Computer Systems and Robotics, University of Karlsruhe, Germany, as a Humboldt Research Fellow. In 1998, he joined Nara Institute of Science and Technology (NAIST), Nara, Japan, and is currently a Professor of Robotics Laboratory in the Graduate School of Information Science. His research interests include human-robot interaction, dexterous manipulation, and biologically inspired robotics.